Analysis and Design of an LCL–T Resonant DC–DC Converter for Underwater Power Supply

Tarak Saha, *Member, IEEE*, Anindya Chitta Bagchi, *Member, IEEE*, and Regan Andrew Zane, *Senior Member, IEEE*

***Abstract*—Constant dc current distribution is preferred over dc voltage distribution in under-sea power distribution networks due to ruggedness over long distance cable impedance and faults. DC–DC converters with constant current input have different design constraints from their constant voltage input counterparts. Considering these constraints, an LCL–T resonant network based isolated dc–dc converter is analyzed in this article to operate as a load independent constant voltage source when supplied with constant dc current at the input. It is shown that use of passive rectification for this converter can limit converter operating load range, which is overcome through use of an active rectifier. A three-angle modulation strategy for a dual-active bridge (DAB) based LCL–T resonant converter is presented to achieve minimum VA rating for tank elements, transformer and the bridges. Detailed analysis and design method are provided for a converter regulating its output voltage at 150 V fed from a 1 A source, operating with 250 kHz switching frequency, over the load range of 50 to 500 W. Experimental results from prototype hardware are presented to show the accuracy of the analysis.**

***Index Terms*—DC current distribution, LCL–T resonant converter, dual active bridge (DAB), DAB–LCL, three angle modulation, constant voltage characteristics.**

I. Introduction

RESONANT power converters are a popular choice for dc–dc power conversion at high switching frequency due to their soft-switching capability, high efficiency, high power density, and low EMI [1]. Because of these inherent advantages, resonant converters are widely used in various applications such as telecom [2], energy storage [3], undersea dc distribution network [4]–[8], wireless power transfer system [9]–[12], battery or capacitor charging [13]–[19], and LED drivers [20]–[22].

In long distance underwater ocean observatory systems [4]–[8], [23]–[24], converters placed on the seabed are distant from the source and a constant dc current based power distribution is preferred because of its robustness against cable impedance and faults. A block diagram of such a distribution network is shown in Fig. 1, where the onshore power source drives a constant current through the trunk cable to m series connected, isolated dc–dc converter module(s) that are contained in their respective hermetically sealed enclosures following IP68 standards and thus the components do not come in contact with the sea-water. Utilizing the conductivity of saline water, the cable current returns to the source through seawater. Each dc–dc converter taps power from this constant current source to regulate its output voltage or current.

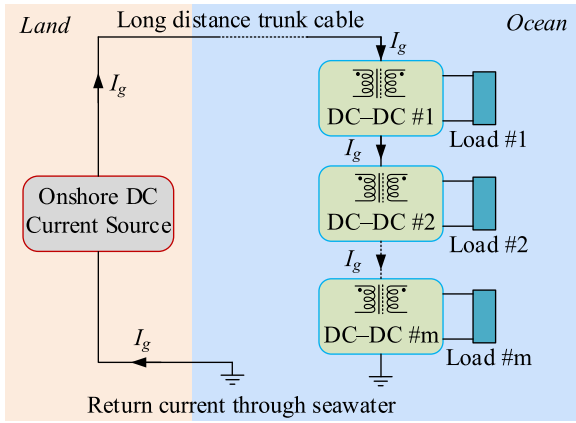

Fig. 1. Underwater dc distribution network fed from onshore dc current source.

With current source as input, converters in [25], [26] employed a current fed inverter (CFI) stage at front end that can operate with zero current switching (ZCS). However, achieving zero voltage switching (ZVS) is challenging in CFI, limiting the switching frequency of operation. With resonant topologies, switches in a CFI must be rated for a value higher than average dc input voltage, which makes the CFI stage impractical for low-current high-voltage systems as mentioned in [7], [8]. Hence, a voltage fed inverter stage is used at the front end, where the dc input voltage varies with the load.

For systems with constant dc current input, the authors in [5] presented a series resonant converter (SRC) based topology to achieve load independent output current. If this SRC is used for output voltage regulation, the variation of control angle will be large for wide load variation and thus will result in high component stress and inferior power conversion efficiency. Authors in [27] used a nonresonant converter based on isolated push-pull converter followed by a boost stage to regulate the output voltage with PWM feedback. And in [7], [8] used a parallel resonant converter (PRC) based topology to achieve

Manuscript received June 3, 2020; revised September 3, 2020; accepted October 12, 2020. Date of publication October 28, 2020; date of current version February 5, 2021. Recommended for publication by Associate Editor G. Moschopoulos. *(Corresponding author: Tarak Saha.)*

The authors are with the Utah State University, Logan, UT 84341 USA (e-mail: taraksaha.ee@gmail.com; bagchi.ee.j@gmail.com; regan.zane@usu.edu).

Color versions of one or more of the figures in this article are available online at https://ieeexplore.ieee.org.

Digital Object Identifier 10.1109/TPEL.2020.3034298

constant current input to constant output voltage. In this paper, an LCL-T resonant network based dc–dc converter is analyzed and it is shown that with suitable design, this converter can produce a load independent, constant output voltage characteristic when powered from a constant dc current source input. The isolation transformer and secondary side devices in PRC presented in [7], [8] have a peak voltage stress 1.6 times the dc output voltage whereas, in LCL-T resonant converter, these components' peak voltage stress equals the dc output voltage (V_{out}). In addition, PRC needs an inductor-capacitor filtering stage at its output whereas, in the LCL-T resonant tank based topology, only capacitive filter is needed at the output. These benefits of LCL-T resonant converter lead to smaller sized passive components, as compared to PRC.

Converters employing an LCL-T resonant tank are presented in [13]–[22], [28]–[30], to achieve a current source behavior from a dc voltage source input and authors in [31] have presented a DAB LCL-T resonant dc–dc converter with voltage sources, both input and output. However, the source of power in underwater dc distribution system is from a constant current source. In [32], an LCL-T resonant tank based non-isolated, dc–dc converter is presented for dc current source to dc voltage source application, but, without a design method. Hence, a detailed analysis and design methodology for an isolated LCL-T resonant converter that converts a dc current source input to a dc voltage source output is needed, which is presented in this article.

The remainder of this article is organized as follows. Steady state modeling and analysis of the converter with a diode bridge rectifier on the secondary side is presented in Section II. A detailed design procedure of an LCL-T resonant tank and transformer turns ratio selection are presented in Section III. The limitations of operation with a diode bridge secondary are shown in Section IV and compared with the solution of a DAB LCL-T resonant converter. Section V contains the details of the hardware prototype development and experimental results, verifying the theoretical analysis.

II. Steady State Modeling and Analysis

Fig. 2(a) shows an LCL-T resonant tank based topology that converts constant dc input current to constant dc output voltage. MOSFETs $Q_1 - Q_4$ form the primary side inverter that operates with symmetrical phase shift modulation with leg *A* leading leg *B* by an angle φ_{AB}, as shown in Fig. 2(b). This inverter translates the dc bus voltage V_{in} to a quasi-square wave v_{AB} and drives the LCL-T resonant tank network formed by inductors L_r, L_g, and capacitor C_r. The resonant tank is followed by an n:1 isolation transformer, output of which is rectified by secondary side diode bridge rectifier consisting of diodes $D_1 - D_4$. The final dc output is filtered through filter capacitor C_f before going to the load, which is represented as a resistor R_{load}. For the analysis to follow, it is assumed that all the components are ideal and lossless.

With fundamental harmonics approximation (FHA) [1], the converter shown in Fig. 2(a) can be drawn as the equivalent

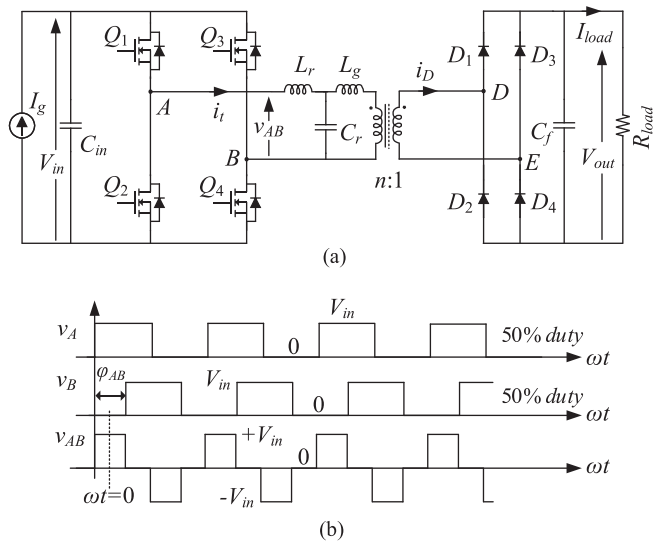

Fig. 2. (a) LCL-T resonant dc–dc converter topology and (b) its primary side inverter modulation.

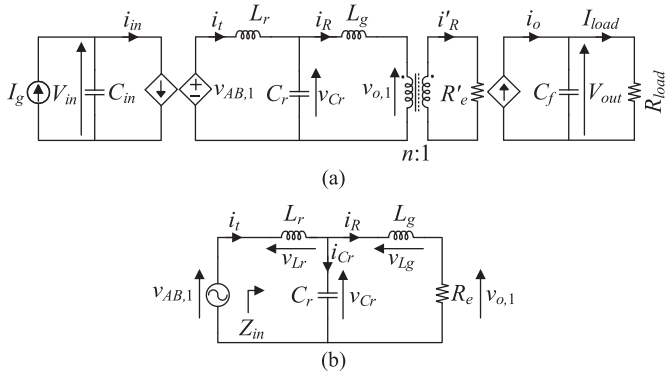

Fig. 3. (a) Equivalent circuit of LCL-T resonant converter and (b) simplified equivalent circuit for steady state analysis using FHA.

circuit shown in Fig. 3(a), where

$$I_g = \langle i_{in} \rangle = \frac{2I_t}{\pi} \sin\left(\frac{\varphi_{AB}}{2}\right) \cos\left(\varphi_{in}\right) \tag{1}$$

$$v_{AB,1} = \frac{4}{\pi} V_{in} \sin\left(\frac{\varphi_{AB}}{2}\right) \cos\left(\omega_s t\right) \tag{2}$$

$$I_{load} = \langle i_o \rangle = \frac{2}{\pi} I'_R \tag{3}$$

and the ac equivalent load resistance is given by

$$R'_e = \frac{8}{\pi^2} R_{load}, \quad R_e = \frac{n^2 8}{\pi^2} R_{load}. \tag{4}$$

In (1) – (4), ω_s is the angular switching frequency, the average value of signal x is represented by $\langle x \rangle$, the amplitude of ac side signal x_y is represented by X_y and the signal or parameter x reflected to the secondary side of the transformer are expressed with a prime (x'). In (1), φ_{in} is the angle between fundamental component of primary side inverter output voltage and current, which is given as

$$\varphi_{in} = \angle Z_{in} \tag{5}$$

where Z_{in} is input impedance of the loaded resonant tank, seen from the primary inverter side, as depicted in Fig. 3(b). Also, Fig. 3(b) shows the simplified ac equivalent circuit of the converter, reflected to the primary side of the transformer.

From the circuit in Fig. 3(b), the output to input voltage transfer function can be derived as

$$\frac{v_{o,1}(s)}{v_{AB,1}(s)} = \frac{1}{1+(1+g)\dfrac{s}{Q\omega_o}+\dfrac{s^2}{\omega_o^2}+g\dfrac{s^3}{Q\omega_o^3}} \tag{6}$$

with the parameters are defined as,

$$\omega_o = \frac{1}{\sqrt{L_rC_r}},\quad Z_o = \sqrt{\frac{L_r}{C_r}},\quad g = \frac{L_g}{L_r},\quad Q = \frac{R_e}{Z_o},\quad F = \frac{f_s}{f_o} \tag{7}$$

where Z_o is the characteristic impedance of the resonant tank, Q is the quality factor of the loaded tank, f_s is the switching frequency of operation, f_o is the resonant frequency of L_r and C_r, and ω_o is the angular resonant frequency.

The amplitude of the ac voltages in Fig. 3(b) are given in terms of dc input and output voltage as

$$|v_{AB,1}| = \frac{4}{\pi}V_{in}\sin\left(\frac{\varphi_{AB}}{2}\right),\quad |v_{o,1}| = \frac{4n}{\pi}V_{out}. \tag{8}$$

For systems with constant dc voltage source, the dc output voltage can be found using (6) and (8), evaluating the magnitude from (6) with $s = j\omega_s$ and is given as

$$V_{out}|_{DC\_Vin} = \frac{V_{in}}{n}\frac{Q\sin\left(\dfrac{\varphi_{AB}}{2}\right)}{\sqrt{Q^2\left(1-F^2\right)^2+\left[(1+g)F-gF^3\right]^2}}. \tag{9}$$

However, for systems with dc current source, V_{in} is dependent on load and expression of V_{out} from (9) cannot be used as it is. The output voltage for such system is derived from the equivalent circuits shown in Fig. 3.

The ac active power drawn from the inverter, which equals the dc input and output power of the lossless converter, are given as

$$P_{AC} = \frac{V_{AB,1,rms}^2}{|Z_{in}|}\cos(\varphi_{in}),\quad P_{in} = V_{in}I_g,$$
$$P_{out} = \frac{V_{out}^2}{R_{load}} \tag{10}$$

where $V_{AB,1,rms}$ is the rms value of the fundamental component of inverter output voltage $v_{AB,1}$, as given in (2). With lossless power conversion, from (10), the input voltage can be expressed as

$$V_{in} = \frac{V_{out}^2}{I_gR_{load}}. \tag{11}$$

Equating the dc output power to the ac active power in (10) and using expressions from (1)–(2) and (11), the dc output voltage can be derived as

$$V_{out} = \frac{\pi^2}{8n}\frac{Z_oI_g}{\sin\left(\dfrac{\varphi_{AB}}{2}\right)}\sqrt{\frac{Q}{\cos(\varphi_{in})}\frac{|Z_{in}|}{Z_o}} \tag{12}$$

and the input impedance, whose derivation is provided in the Appendix, is given by

$$Z_{in} = \frac{Z_o}{\left[\left(1-gF^2\right)^2+F^2Q^2\right]}\left[Z_R+jZ_I\right] \tag{13}$$

where expression for Z_R and Z_I are presented in the Appendix.

The analysis presented in this section establishes the steady state relations between dc input and output for an LCL-T resonant converter, with its dependence on tank parameters and operating point, which is used in next section for design of the converter.

III. Design of LCL-T Resonant Converter

The dc output voltage of the converter, derived in (12), is dependent on the resonant tank parameters, load, operating frequency etc. In this section, it will be shown how the converter is designed, with proper choice of operating point, to achieve load independent output voltage from constant current input. With further analysis, a design method to optimize tank components and transformer turns ratio, is also presented in this section.

A. Operating Point Selection

From the expression of dc output voltage in (12), it can be normalized to be expressed as

$$V_{out\_norm} = \sqrt{\frac{Q}{\cos(\varphi_{in})}|Z_{in\_norm}|} \tag{14}$$

which is normalized with a base voltage defined as

$$V_{base} = \frac{\pi^2}{8n}\frac{Z_oI_g}{\sin\left(\dfrac{\varphi_{AB}}{2}\right)} \tag{15}$$

and the normalized Z_{in} is defined as

$$Z_{in\_norm} = \frac{Z_{in}}{Z_o}. \tag{16}$$

The normalized dc output voltage (V_{out_norm}) from (14) is plotted against normalized switching frequency (F) in Fig. 4(a) for various loads (Q), with $g = 1$. It can be seen that V_{out_norm} becomes independent of Q if the switching frequency of operation is selected to be equal to the resonant frequency, *i.e.*, with $F = 1$. Under this operating condition, the expression of output voltage from (12) is now given as

$$V_{out}|_{F=1} = \frac{\pi^2}{8n}\frac{Z_oI_g}{\sin\left(\dfrac{\varphi_{AB}}{2}\right)}. \tag{17}$$

From (17), it can be seen that with $F = 1$, V_{out} is also independent of g (L_g), which is shown by V_{out_norm} versus F plot in Fig. 4(b), for various Q, with an arbitrarily chosen value of $g = 0.3$. A special case of $g = 0$ makes it a parallel resonant converter, achieving load independent output voltage from a constant current source input [7], [8].

From the plots in Fig. 4, it can be observed that the output voltage is almost load independent within $\pm 10\%$ of $F = 1$. So, it is possible to operate the converter with a small variation in

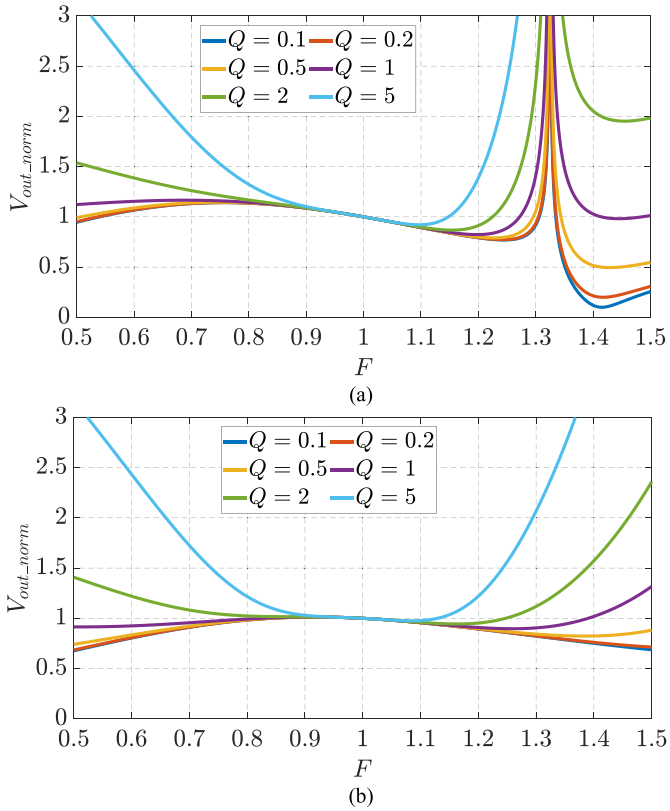

Fig. 4. Steady state normalized dc output voltage (V_{out_norm}) versus normalized switching frequency (F), for different load (Q), (a) with $g = 1$ and (b) with $g = 0.3$.

F around 1, in addition to phase shift control. However, with a small variation limit in F, the transient response can get limited, depending on the magnitude of load transient, due to low margin from steady state operating point to controller output limit. Moreover, since the converters are part of a system of converters with common source, if they are controlled though F variation then different converters will operate at different switching frequencies, depending on their individual loads, which will introduce low frequency (difference in frequency among converters) ripple component injected to the source which is challenging for filter design. Hence all the converters are designed to operate at fixed frequency and controlled through phase shift modulation.

With $F = 1$, the tank input impedance (Z_{in}) from (13) can be derived as

$$Z_{in}|_{F=1} = \frac{Z_o}{\sqrt{Q^2 + (1-g)^2}} \angle \tan^{-1}\left(\frac{1-g}{Q}\right). \tag{18}$$

From this expression of Z_{in}, if $g < 1$, φ_{in} is positive and thus Z_{in} becomes inductive, which can help achieving ZVS for the primary side inverter switches. However, a nonzero φ_{in} puts a restriction on minimum power operation of the converter for which its output can be regulated [4]–[6]. Hence, g is selected to be equal to unity and with $g = 1$, Z_{in} becomes resistive, making the primary side inverter operate at unity power factor (UPF), considering FHA. With $F = 1$ and $g = 1$, Z_{in} from (18) can be

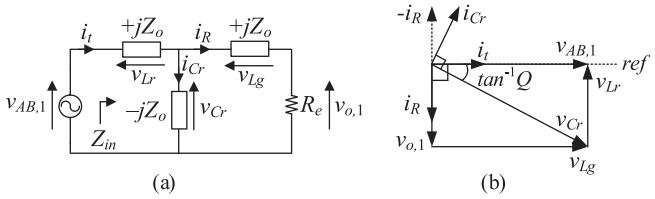

Fig. 5. (a) Equivalent circuit of the tank, at operating point of $F = 1$ and $g = 1$ and (b) phasor diagram for the AC signals from this equivalent circuit.

given as

$$Z_{in}|_{F=1,\, g=1} = \frac{Z_o^2}{R_e} \angle 0^{\circ}. \tag{19}$$

B. Derivation of Tank Signals

With the selected operating point of $F = 1$ and $g = 1$, the tank ac circuit in Fig. 3(b) can be simplified and redrawn as shown in Fig. 5(a). This circuit is solved analytically to derive the ac signals of the tank. The solutions are provided in this section. The phasor diagram of the ac quantities from Fig. 5(a) is drawn in Fig. 5(b), considering the fundamental component of v_{AB} as reference.

From the equivalent circuit in Fig. 3(a), the current (i_t) in the inductor L_r can be found by balancing the dc input current and rectified average current at the primary side inverter. Since the inverter is operating at UPF, i_t can be expressed as

$$i_t(t) = \frac{\pi}{2} \frac{I_g}{\sin\left(\frac{\varphi_{AB}}{2}\right)} \cos(\omega_s t). \tag{20}$$

The resonant tank ac output voltage $v_{o,1}$ can be found from the fundamental component of ac input voltage to the secondary side diode bridge rectifier, reflected to the transformer primary side, and is given by

$$v_{o,1}(t) = \frac{4n}{\pi} V_{out} \cos\left(\omega_s t - \frac{\pi}{2}\right). \tag{21}$$

Similarly, the current (i_R) in the load side inductor L_g, connected to the secondary side diode bridge rectifier, can be given by

$$i_R(t) = \frac{\pi}{2n} I_{load} \cos\left(\omega_s t - \frac{\pi}{2}\right). \tag{22}$$

The voltage across and current through the resonant capacitor are given by

$$v_{Cr}(t) = \frac{4n}{\pi} V_{out} \sqrt{1 + \frac{1}{Q^2}} \cos(\omega_s t - \tan^{-1} Q) \tag{23}$$

$$i_{Cr}(t) = \frac{4n}{\pi} \frac{V_{out}}{Z_o} \sqrt{1 + \frac{1}{Q^2}} \cos\left[\omega_s t + \tan^{-1}\left(\frac{1}{Q}\right)\right]. \tag{24}$$

The detailed derivation of the tank signals can be found in the Appendix.

C. RMS Values and VA of Tank Components

From (20)–(24) the rms values of tank signals can be found out as

$$I_{t,rms} = \frac{\pi}{2\sqrt{2}} \frac{I_g}{\sin\left(\frac{\varphi_{AB}}{2}\right)} \tag{25}$$

$$I_{R,rms} = \frac{\pi}{2\sqrt{2}n} I_{load} \tag{26}$$

$$V_{Cr,rms} = \frac{2\sqrt{2}n}{\pi} V_{out} \sqrt{1 + \frac{1}{Q^2}} \tag{27}$$

$$I_{Cr,rms} = \frac{2\sqrt{2}n}{\pi} \frac{V_{out}}{Z_o} \sqrt{1 + \frac{1}{Q^2}}. \tag{28}$$

From (25)–(28), it can be observed that for a given operating condition (I_g, V_{out}, φ_{AB}), the rms current of the source side resonant inductor (L_r) is constant and independent of load whereas, rms current in load side resonant inductor (L_g) is directly proportional to load (I_{load}). RMS voltage and current of the resonant capacitor is also dependent on the load (Q).

From these rms current(s), referring to the circuit in Fig. 5(a), the VA for the resonant tank components can be determined. The VA for L_r can be evaluated as

$$VA_{Lr} = I_{t,rms}^2 Z_o = QP_{out} \tag{29}$$

and the VA for L_g is evaluated to be

$$VA_{Lg} = I_{R,rms}^2 Z_o = \frac{P_{out}}{Q}. \tag{30}$$

Details of (29) and (30) are provided in the Appendix. The VA of the resonant capacitor can be found using (28) and is expressed as

$$VA_{Cr} = I_{Cr,rms}^2 Z_o. \tag{31}$$

Now, from the phasor diagram of Fig. 5(b), it can be seen that i_t and i_R in quadrature and i_{Cr} is the phasor subtraction of i_t and i_R. Hence, (28) can also be expressed as

$$I_{Cr,rms} = \sqrt{I_{t,rms}^2 + I_{R,rms}^2} \tag{32}$$

and using (32), (31) can be written as

$$VA_{Cr} = (I_{t,rms}^2 + I_{R,rms}^2) Z_o = \left(Q + \frac{1}{Q}\right) P_{out}. \tag{33}$$

It can be seen from (29), (30) and (33), that the VA of the tank capacitor is the sum of VA of the tank inductors. The total VA of the tank is calculated by summing up (29), (30) and (33), and is given by

$$VA_{tank} = 2\left(Q + \frac{1}{Q}\right) P_{out}. \tag{34}$$

D. Design of Resonant Tank

To find the VA rating of the resonant tank, (34) needs to be evaluated at maximum output power (P_{out_max}). The normalized VA rating (VA_{tank_norm}), with respect to P_{out_max} can be given from (34) as

$$VA_{tank\_norm} = 2\left(Q_{Pout\_\max} + \frac{1}{Q_{Pout\_\max}}\right) \tag{35}$$

where Q_{Pout_max} is the quality factor at maximum output power. It can be seen that the minimum value of VA_{tank_norm} from (35) is attained at

$$Q_{Pout\_\max} = \frac{1}{Q_{Pout\_\max}} = 1 \tag{36}$$

and the minimum value of total tank VA rating is found out using (34) and (36) and it is given as

$$VA_{tank\_min} = 4P_{out\_max}. \tag{37}$$

In order to design the tank elements, we need to start at (17) where V_{out} and I_g are known, but, n, Z_o and φ_{AB} are to be decided on. From the expression of Q in (7) and P_{out} from (10), the characteristic impedance of the tank can be written as

$$Z_o = \frac{8n^2}{\pi^2} \frac{V_{out}^2}{P_{out}Q}, \tag{38}$$

and substituting Z_o from (38) into (17), the transformer turns ratio can be expressed as

$$n = \frac{P_{out}Q \sin\left(\frac{\varphi_{AB}}{2}\right)}{I_g V_{out}}. \tag{39}$$

In order to achieve minimum VA rating for the tank, the optimum value of transformer turns ratio ($n_{min\cdot VA}$) can be found by substituting $Q = Q_{Pout\_max} = 1$ from (36) into (39), and is given by

$$n_{min\_VA} = \frac{P_{out\_max} \sin\left(\frac{\varphi_{AB}}{2}\right)}{I_g V_{out}}. \tag{40}$$

The value of φ_{AB} is selected to be 120° which produces least harmonic content at the output of the inverter with no triplen harmonics [31]. This also provides sufficient margin from the maximum possible control angle of 180° to support transient response. After determining the transformer turns ratio from (40), Z_o is evaluated from (38) as

$$Z_o = \frac{8n_{min\_VA}^2}{\pi^2} \frac{V_{out}^2}{P_{out\_max}} \tag{41}$$

and from (7), the tank element values can be calculated as

$$L_r = \frac{Z_o}{2\pi f_o} = \frac{Z_o}{2\pi f_s} \tag{42}$$

$$C_r = \frac{1}{2\pi f_o Z_o} = \frac{1}{2\pi f_s Z_o} \tag{43}$$

$$L_g = L_r = \frac{Z_o}{2\pi f_s}. \tag{44}$$

And, the ratings of the resonant tank elements are given in (25)–(28). With these design equations, the resonant tank and transformer turns ratio can be uniquely designed with minimum VA rating. However, designing the tank with minimum VA rating can result in discontinuous current in the secondary diodes,

TABLE I
RESONANT TANK PARAMETERS

L_r [μH]	C_r [pF]	L_g [μH]	n
194.4	2085	194.4	2.9

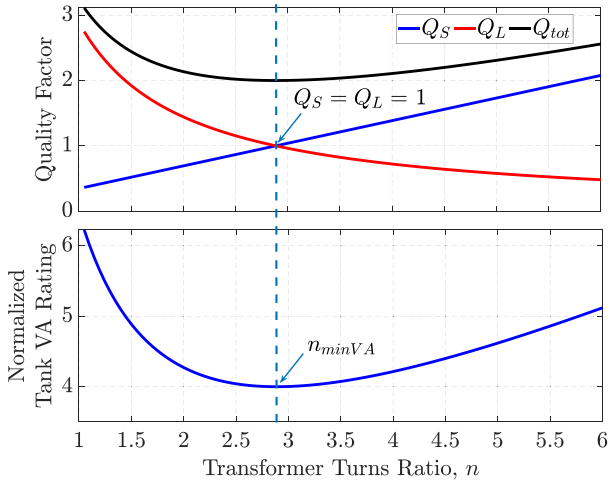

Fig. 6. Quality factor of the tank elements (top) and normalized VA rating of the tank (bottom) with respect to transformer turns ratio.

which can possibly limit the range of load for which converter output voltage can be regulated. This can be overcome by replacing diode bridge with an active bridge on the secondary side of the converter, which is presented in the next sections with simulation and experimental results.

IV. Dual-Active Bridge LCL-T Resonant Converter

With the design method from Section III–D, the converter is designed for a system with 1 A input and 150 V output with a load range of 50 to 500 W. The designed parameters are listed in Table I. The plot of quality factor and normalized tank VA rating for various transformer turns ratio is presented in Fig. 6, where it can be seen that the tank VA is minimum at $n = n_{min\_VA}$ as per (40). In Fig. 6, the quantities Q_S, Q_L, and Q_{tot} are defined as follows

$$Q_S = Q, \quad Q_L = \frac{1}{Q}, \quad Q_{tot} = Q_S + Q_L. \tag{45}$$

Details of (45) can be found in the Appendix.

A. Limitation With Diode-Bridge Rectifier

With the tank parameters listed in Table I, the converter of Fig. 2(a) is simulated in MATLAB/PLECS and the steady state dc output voltage over the load range is plotted in Fig. 7.

It can be seen from the blue plot in Fig. 7 that the output voltage with secondary side diode bridge rectifier does not stay constant, independent of load and increases in value as the load reduces. Since the tank is designed for minimum VA, the diodes operate in discontinuous conduction mode (DCM) due to low quality factor. This increase in V_{out} at light load will demand the control angle (φ_{AB}) to go towards its limit of 180°, to keep the output voltage at its desired value. This can potentially hinder

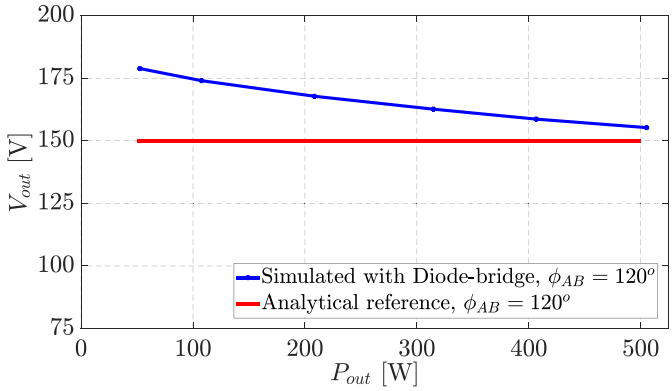

Fig. 7. Steady state dc output voltage (V_{out}) versus load power (P_{out}); red: result from analysis, blue: simulation result with diode-bridge.

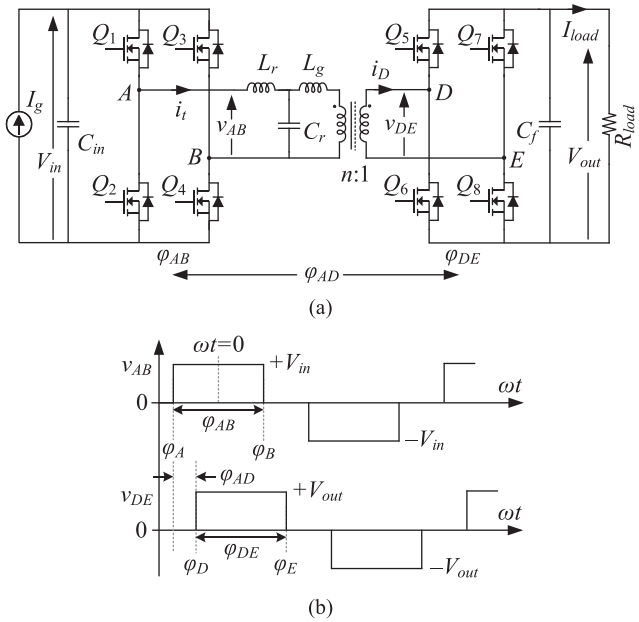

Fig. 8. (a) DAB LCL-T resonant dc–dc converter topology and (b) its modulation waveforms.

the load range of operation for which the converter can regulate its output. In order to keep the diodes in continuous conduction mode (CCM) over a load range, the tank components have to be designed with higher VA rating which will increase the size of the converter. Alternately, the converter can be designed with lower nominal value of φ_{AB}, considering the load range and margin for component tolerances, but this will lead to higher component stress (25)–(28) and losses.

B. Secondary Side Active Rectification

To operate the converter with wide range load regulation, it is essential to keep the secondary bridge in CCM. This is achieved by employing an active bridge on the secondary side, as shown in Fig. 8(a). The modulation scheme for both primary and secondary bridges is depicted in Fig. 8(b), where φ_{DE} is the control angle between legs D and E of secondary bridge, and φ_{AD} is the angle between legs A and D.

With a secondary active bridge, the current in L_g and in the transformer secondary will be in CCM. To operate the

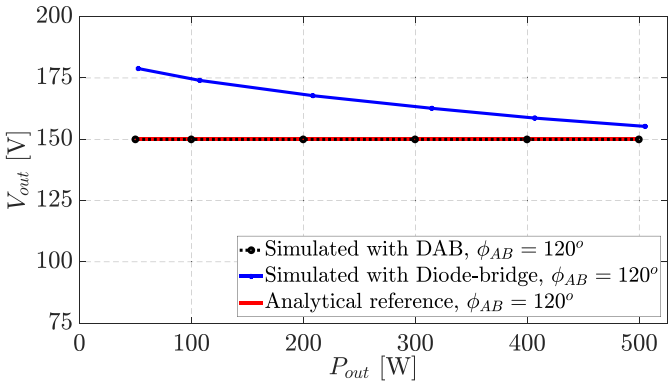

Fig. 9. Steady state dc output voltage (V_{out}) versus load power (P_{out}); red: result from analysis, blue: simulation result with diode-bridge, black: simulation result with DAB.

secondary bridge at unity power factor (with FHA) and emulate the behavior of diode rectifier, the secondary bridge modulation angle φ_{DE} should be equal to 180°. From the phasor diagram shown in Fig. 5(b), the relationship among the three modulation angles [φ_{AB}, φ_{AD}, φ_{DE}] can be given as

$$\varphi_{AD} = \frac{\varphi_{AB}}{2} + \frac{\pi}{2} - \frac{\varphi_{DE}}{2} \tag{46}$$

and with $\varphi_{DE} = 180°$, (46) becomes

$$\varphi_{AD} = \frac{\varphi_{AB}}{2}. \tag{47}$$

The DAB LCL-T converter is also simulated in MATLAB/PLECS and the steady state dc output voltage at various load is plotted in Fig. 9, with the tank parameters presented in Table I. This is also compared with the result achieved with a diode-bridge on the secondary side and is shown in blue on the same plot. From the black plot in Fig. 9, it can be seen that the steady state dc output voltage remains constant, independent of load, as derived in (17), matching the analytical reference plot in red.

V. Experimental Verification

A prototype hardware has been built to verify the analysis presented so far with the tank parameters mentioned in Table I and additional details presented in Table II. The converter is designed to operate at 250 kHz switching frequency, which is the operating frequency of all the series connected converters used in this underwater dc current distribution network. The prototype is designed for operation up to 500 W with 150 V dc output voltage and it is tested over 10:1 load range for experimental verification. The photograph of the test setup is shown in Fig. 10. With operation at $F = 1$ and $g = 1$, both the primary and secondary inverter(s) operate with its fundamental voltage and current in phase which means that all the switches in the converter will not have ZVS by the tank current. On the primary side inverter, leg *B* MOSFETs go through ZVS by tank current and an active ZVS assisting circuit is used for leg *A* [33]. Since the secondary side bridge operates at unity power factor with fixed dc output voltage, a fixed, passive inductor (L_{zvs_sec}) is used for ZVS [34] of secondary side MOSFETs. Further details

TABLE II
Converter Details

Component / Parameter	Value
I_g (A)	1
V_{out} (V)	150
f_s (kHz)	250
P_{out} (W)	50 – 500
Primary MOSFETs	C2M1000170D
$C_{DC\ pri}$ (μF)	0.23
$L_{zvs\ pri}$ (μH)	50
Secondary Diode(s)	FFSH2065B-F085
Secondary MOSFETs	IXFQ72N20X3
$C_{DC\ sec}$ (μF)	6.4
$L_{zvs\ sec}$ (μH)	60

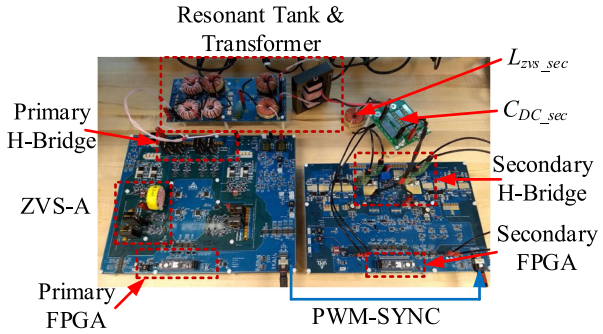

Fig. 10. Photograph of the hardware test setup.

of the ZVS assisting circuit can be found in [35]. DC blocking capacitors (C_{DC_pri} and C_{DC_sec}) are used in both primary and secondary side H-bridges to block any dc component of voltage arriving out of the H-bridges due to any component mismatch. The value(s) of the dc blocking capacitor(s) is chosen significantly higher than the resonant capacitor such that it does not impact the overall capacitor seen from the resonant inductor terminals and thus does not influence the resonant frequency of the tank.

First, the converter is tested with a diode bridge rectifier and the results are shown in Fig. 11 for 50 W and 500 W operation with $\varphi_{AB} = 120°$. It can be seen from the v_{DE} (purple) and i_D (green) plot in Fig. 11(a) that the diode operates in DCM mode. Then the converter is tested with active rectifier (DAB) and the steady state operating waveforms are shown in Fig. 12 for 50 W and 500 W operation with $\varphi_{AB} = 120°$, keeping $\varphi_{DE} = 180°$ and $\varphi_{AD} = 60°$. In addition, the gate-source and drain-source voltage across the bottom switch(es) of all the H-bridge legs of DAB LCL-T are presented in Fig. 13 at minimum (50 W) and maximum (500 W) load. From this results in Fig. 13, it can be seen that the drain-source voltage of the switch(es) falls to zero, before its gate-source voltage rises, confirming ZVS operation over the entire load range. And, due to half wave symmetry in operation, the top switches also go through ZVS turn on.

The steady state dc output voltage results, with both a diode bridge and an active bridge secondary, are plotted in Fig. 14, versus the load power, at fixed $\varphi_{AB} = 120°$. In Fig. 14, the red plot is the analytical reference (150 V) and the blue

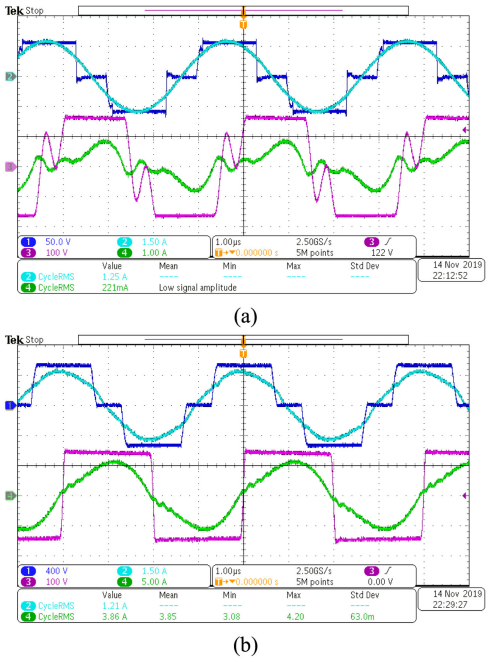

Fig. 11. Steady state operating waveforms with diode-bridge on the secondary side with $\varphi_{AB} = 120°$, (a) at 50 W and (b) at 500 W. CH1 (deep blue): v_{AB}, CH2 (cyan): i_t, CH3 (purple): v_{DE}, CH4 (green): i_D.

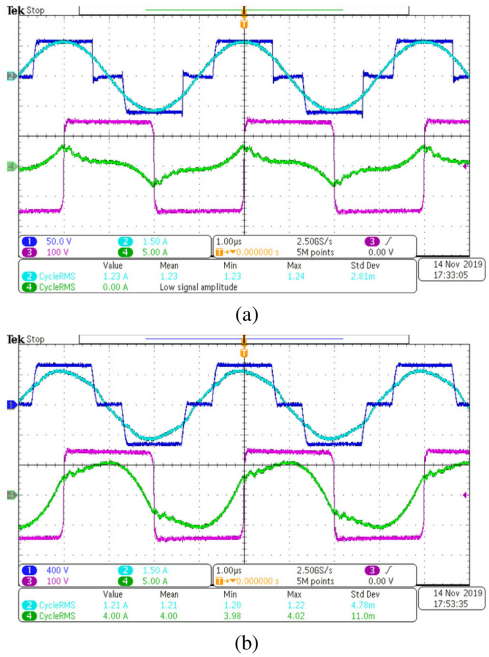

Fig. 12. Steady state operating waveforms with active bridge on the secondary side with $\varphi_{AB} = 120°$, $\varphi_{DE} = 180°$ and $\varphi_{AD} = 60°$, (a) at 50 W and (b) at 500 W. CH1 (deep blue): v_{AB}, CH2 (cyan): i_t, CH3 (purple): v_{DE}, CH4 (green): i_D.

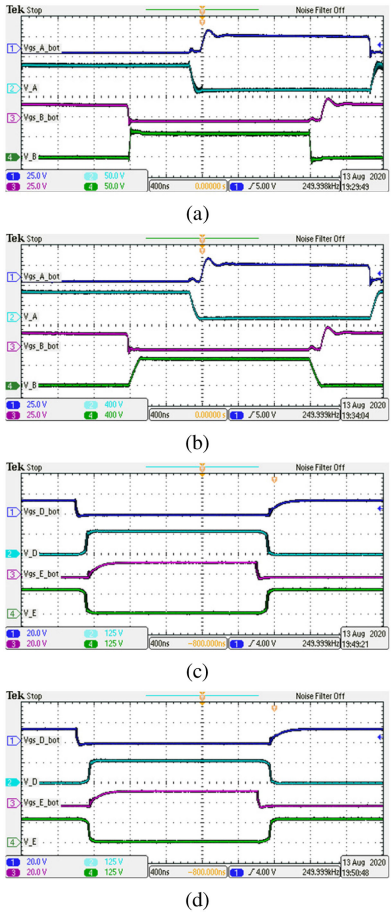

Fig. 13. Gate-source and drain-source waveforms of bottom switch(es) of all the legs of primary H-bridge at (a) 50 W and (b) 500 W, and secondary H-bridge at (c) 50 W and (d) 500 W, operated with $\varphi_{AB} = 120°$, $\varphi_{DE} = 180°$ and $\varphi_{AD} = 60°$, showing ZVS operation.

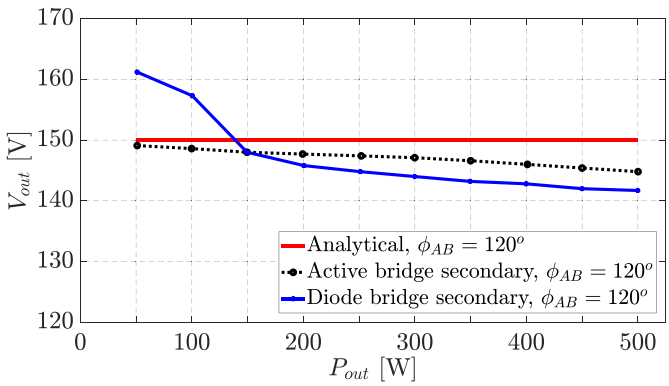

Fig. 14. Steady state dc output voltage (V_{out}) versus load power (P_{out}) with $\varphi_{AB} = 120°$. Red: result from analysis, blue: experimental result with diode-bridge on the secondary, black: experimental result with active bridge on the secondary.

and black traces represent the results with a diode rectifier and an active rectifier, respectively. It can be seen that the output voltage is not load independent for a diode bridge, whereas, with an active secondary bridge, the output voltage is relatively constant over a 10:1 load range. The variation in V_{out} with an active secondary is between 149.1 and 144.8 V, which is only about 2.9%. The variation is due to non-idealities such as ESR of components. The results presented here are from 50 to 500 W that is typical range of load seen by the converter. The converter will ideally maintain its output voltage at the same level while the load power falls further below 50 W. In practice, there could be deviation in output voltage from its ideal value, due

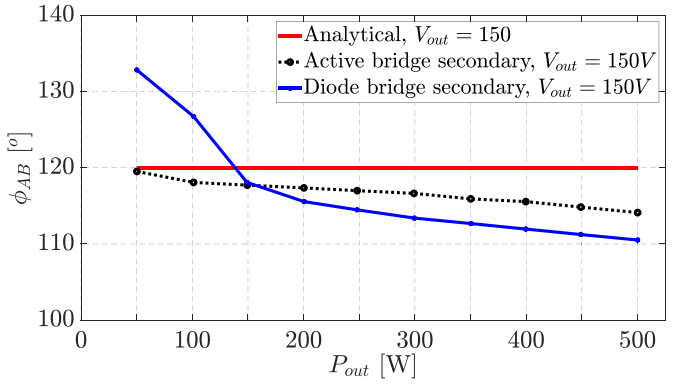

Fig. 15. Variation in control angle φ_{AB} to regulate V_{out} at a fixed value of 150 V, versus load power. Red: result from analysis, blue: experimental result with diode-bridge on the secondary, black: experimental result with active bridge on the secondary.

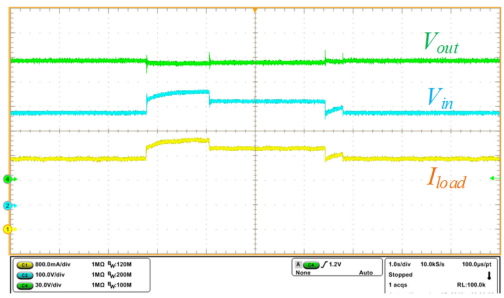

Fig. 16. DAB LCL-T operation under load transient from 350 to 400 W and back to 350 W with fixed $\varphi_{AB} = 115°$. CH1 (yellow): output current (I_{load}), CH2 (cyan): input voltage (V_{in}) and CH4 (green): output voltage (V_{out}).

to component tolerance, temperature variation etc., which will be taken care of by the controller for output voltage regulation. From the hardware results, the variation of V_{out} with a diode bridge is lower than predicted by simulation, which is attributed to the parasitic capacitance of the diodes. Once the diode turns off, the diode capacitance resonates with L_g, which can be seen from v_{DE} (purple) and i_D (green) plot in Fig. 11(a).

The variation of control angle (φ_{AB}) needed to keep the output voltage regulated at 150 V is plotted in Fig. 15, where again the red line shows the analytical prediction and the blue and black traces represent the results with a diode rectifier and an active rectifier, respectively. It can be seen from these plots that variation in φ_{AB} is quite large for operation with a diode bridge, whereas the variation is only 5.4° with active bridge on the secondary, over the 10:1 load range.

The DAB LCL-T resonant converter is also tested with load transient at its output with a fixed control angle ($\varphi_{AB} = 115°$) and the result is shown in Fig. 16. The output load is varied from 350 to 400 W and then back to 350 W. In Fig. 16, the input dc voltage (V_{in}) is captured by CH2 (cyan), output current (I_{load}) is captured by CH1 (yellow) and the output voltage (V_{out}) is captured by CH4 (green). It can be observed from this result that even under load transient the output voltage returns to the same value at steady state.

The rms values of tank inductor current and capacitor voltages are measured from the oscilloscope captures at different loads

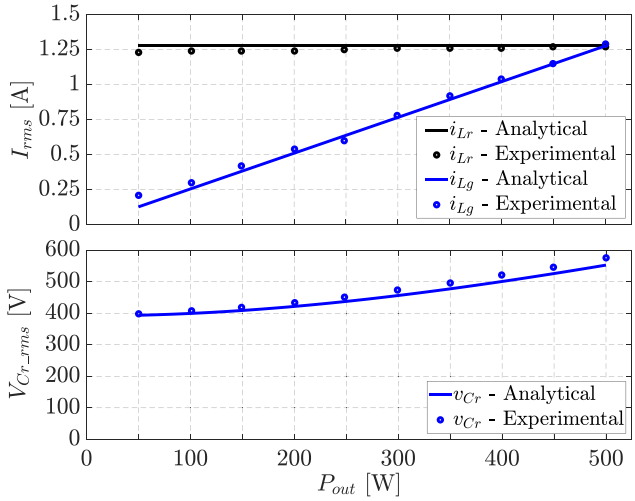

Fig. 17. Comparison of analytical and experimentally measured rms values of tank signals of the DAB LCL-T converter over the load range. Top plot pane: black line is for $I_{t,rms}$ and blue line is for $I_{R,rms}$; bottom plot pane: blue line shows the values for $V_{Cr,rms}$. Solid lines are for analytical and dots are for experimental results.

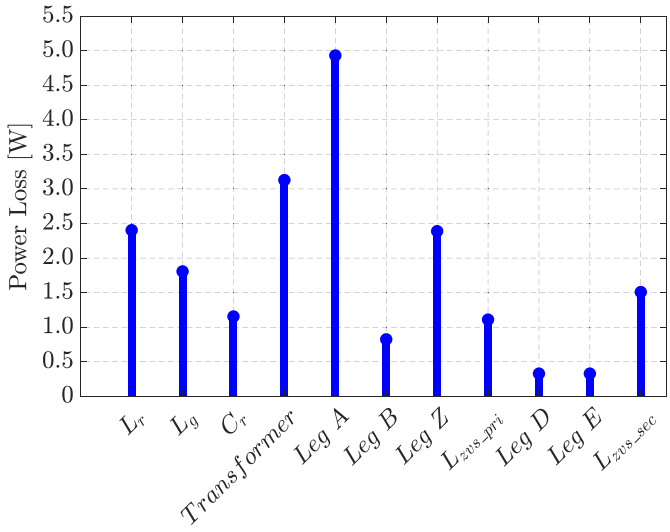

Fig. 18. Power loss distribution among the components of DAB LCL-T converter at full load (500 W).

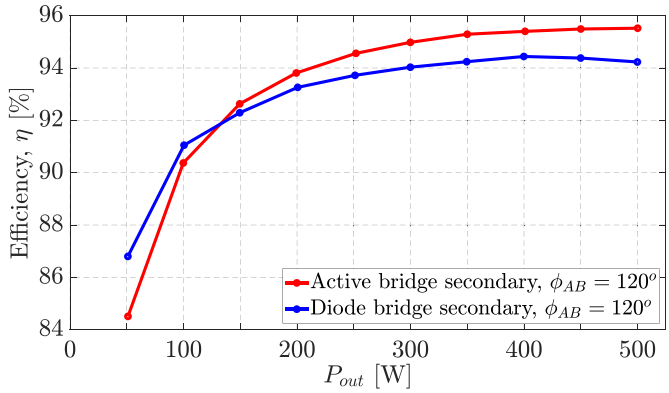

Fig. 19. Efficiency of the converter over the load range, operating at fixed control angle $\varphi_{AB} = 120°$. Blue: experimental result with diode-bridge on the secondary, red: experimental result with active bridge on the secondary.

and are compared with the analytical values derived in (25)–(27). The comparison is shown in Fig. 17, where analytical values are plotted in solid lines and the measured values are shown in corresponding circles of the same color. The top plot in Fig. 17 compares the rms current in the tank inductors and the bottom plot compares the resonant capacitor voltage. The result depicts a good match between experimental result and analysis.

The analytically evaluated power loss in different components of the DAB LCL-T converter is presented in Fig. 18, at full load operating condition. These losses are used for components and heat sink design with natural cooling. The efficiency of the converter, operating at fixed control angle of $\varphi_{AB} = 120°$, with active and passive bridges on the secondary side, are shown in Fig. 19 in red and blue, respectively. It can be seen that the converter operates with a higher efficiency with an active secondary bridge due to the lower conduction loss. The peak efficiency is approximately 96%.

VI. Conclusion

In underwater dc distribution systems, a constant current source is used to power multiple, series-connected converters to achieve robustness against voltage drop over the cable length and cable faults. However, powering from a current source brings in various challenges in converter design. Addressing these challenges, in this paper, it is shown that an LCL-T resonant dc–dc converter can be designed to achieve a load-independent, constant dc output voltage characteristic when powered from a constant dc current source. Detailed modeling, analysis and design are presented for this converter. With analysis, simulation and hardware results, it is shown that diode bridge rectification on the output side of the converter imposes a challenge on low Q (VA rating) design and the use of active bridge overcomes this limitation. A modulation scheme for the DAB LCL-T resonant converter is presented for overall operation of the converter with minimum VA rating for the tank components, the isolation transformer, and the H-bridges. Finally, a hardware prototype is developed and tested for a system with 1 A input current, 150 V output voltage, operating at a switching frequency of 250 kHz, over a load range of 50 to 500 W. Results obtained from hardware experiments confirm the analysis with a good match between analytical expressions and experimentally obtained values.

Appendix

A. Derivation of Tank Input Impedance

With reference to the ac equivalent circuit shown in Fig. 3(b), the impedances of individual tank components are given by

$$X_{Lr} = 2\pi f_s L_r = FZ_o, \quad X_{Lg} = gFZ_o,$$
$$X_{Cr} = \frac{1}{2\pi f_s C_r} = \frac{Z_o}{F} \tag{A.1}$$

where Z_o and F are as defined in (7). Now, the tank input impedance can be derived as

$$Z_{in} = jFZ_o + \frac{-j\frac{Z_o}{F}(R_e + jgFZ_o)}{-j\frac{Z_o}{F} + (R_e + jgFZ_o)} \tag{A.2}$$

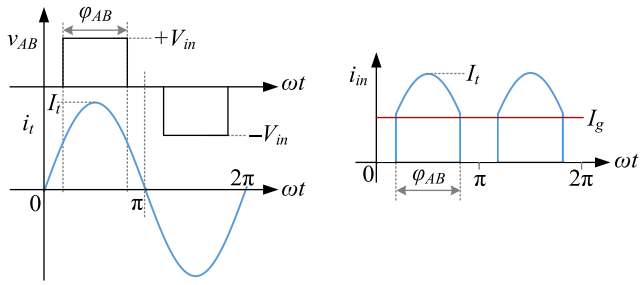

Fig. 20. Primary side inverter's output voltage and current waveform (left) and dc side input current waveform (right).

which can be simplified to

$$Z_{in} = jFZ_o + \frac{Z_o(Q + jgF)}{(1 - gF^2) + jFQ} \tag{A.3}$$

where Q is defined in (7). The expression of Z_{in} from (A.3) can further be expanded to be expressed in the form

$$Z_{in} = \frac{Z_o}{[(1 - gF^2)^2 + F^2Q^2]}[Z_R + jZ_I] \tag{A.4}$$

where Z_R and Z_I are expressed as

$$Z_R = Q(1 - gF^2)(1 - F^2)^2 + (1 + g)QF^2 - gQF^4$$
$$Z_I = (1+g)F(1-gF^2) - gF^3(1 - gF^2) - FQ^2(1 - F^2)^2. \tag{A.5}$$

When operating at resonance, *i.e.*, at $F = 1$, Z_{in} from (A.4) can be simplified to

$$Z_{in}|_{F=1} = \frac{Z_o}{\sqrt{Q^2 + (1 - g)^2}} \angle \tan^{-1}\left(\frac{1 - g}{Q}\right). \tag{A.6}$$

And, the power factor, $\cos(\varphi_{in})$, can be given as

$$\cos(\varphi_{in})|_{F=1} = \frac{Q}{\sqrt{Q^2 + (1 - g)^2}}. \tag{A.7}$$

Substituting (A.6) and (A.7) into (12), the dc output voltage can be expressed as

$$V_{out}|_{F=1} = \frac{\pi^2}{8n}\frac{Z_o I_g}{\sin\left(\frac{\varphi_{AB}}{2}\right)}. \tag{A.8}$$

Further, when g = 1, *i.e.*, with $L_g = L_r$, Z_{in} and $\cos(\varphi_{in})$, are given as

$$Z_{in}|_{F=1,\, g=1} = \frac{Z_o^2}{R_e}\angle 0^o, \quad \cos(\varphi_{in})|_{F=1,\, g=1} = 1. \tag{A.9}$$

B. Derivation of Tank Quantities

In this section, the tank signals are derived from the equivalent circuit shown in Fig. 3(a) and Fig. 5(a). The input current (i_t) to the resonant tank from the inverter is shown in Fig. 20 and its rectified dc side current (i_{in}) is shown on the right hand side of the same figure. Since the average value of i_{in} comes from the dc source (I_g), the amplitude of i_t can be found out through

$$I_g = \langle i_{in} \rangle = \frac{2}{\pi} I_t \sin\left(\frac{\varphi_{AB}}{2}\right), \tag{B.1}$$

where $\langle x \rangle$ denotes average of x over its period. Since the converter is operating at $F = 1$ and $g = 1$, $v_{AB,1}$ and i_t are in phase and thus, using (B.1), the current in the resonant inductor L_r can be expressed as

$$i_t(t) = I_t \cos(\omega_s t) = \frac{\pi}{2} \frac{I_g}{\sin\left(\frac{\varphi_{AB}}{2}\right)} \cos(\omega_s t). \quad \text{(B.2)}$$

The amplitude of load side resonant inductor current (i_R) is evaluated from the circuit in Fig. 5(a) with amplitude of $v_{o,1}$ from (8) and is given as

$$I_R = \frac{|v_{o,1}|}{R_e} = \frac{\frac{4n}{\pi} V_{out}}{\frac{8n^2}{\pi^2} R_{load}} = \frac{\pi}{2n} I_{load}. \quad \text{(B.3)}$$

Now, from the circuit of Fig. 5(a), i_R can be expressed in terms of i_t as

$$i_R = i_t \frac{-jZ_o}{-jZ_o + R_e + jZ_o} = -j\frac{Z_o}{R_e} i_t \quad \text{(B.4)}$$

which means that i_R lags i_t by 90° and thus, using (B.3), $i_R(t)$ can be express as

$$i_R(t) = I_R \cos\left(\omega_s t - \frac{\pi}{2}\right) = \frac{\pi}{2n} I_{load} \cos\left(\omega_s t - \frac{\pi}{2}\right). \quad \text{(B.5)}$$

The voltage across the resonant capacitor can be found from Fig. 5(a) as well and is derived as

$$v_{Cr} = i_R(R_e + jZ_o) = \left[\frac{4n}{\pi}\frac{V_{out}}{R_e} \angle(-\frac{\pi}{2})\right] R_e \left(1 + \frac{j}{Q}\right)$$
$$= \frac{4n}{\pi} V_{out} \sqrt{1 + \frac{1}{Q^2}} \angle\left[-\frac{\pi}{2} + \tan^{-1}\left(\frac{1}{Q}\right)\right]. \quad \text{(B.6)}$$

Using trigonometric identity, it can be shown that

$$\tan^{-1} Q = \frac{\pi}{2} - \tan^{-1}\left(\frac{1}{Q}\right). \quad \text{(B.7)}$$

Hence, from (B.6) the resonant capacitor voltage is given as

$$v_{Cr}(t) = \frac{4n}{\pi} V_{out} \sqrt{1 + \frac{1}{Q^2}} \cos(\omega_s t - \tan^{-1} Q). \quad \text{(B.8)}$$

The current through C_r is evaluated as

$$i_{Cr} = \frac{v_{Cr}}{-jZ_o} = \frac{4n}{\pi}\frac{V_{out}}{Z_o} \sqrt{1 + \frac{1}{Q^2}} \angle\left(-\tan^{-1} Q + \frac{\pi}{2}\right). \quad \text{(B.9)}$$

With the identity shown in (B.7), current in the resonant capacitor is expressed as

$$i_{Cr}(t) = \frac{4n}{\pi}\frac{V_{out}}{Z_o} \sqrt{1 + \frac{1}{Q^2}} \cos\left[\omega_s t + \tan^{-1}\left(\frac{1}{Q}\right)\right]. \quad \text{(B.10)}$$

The VA of L_r is evaluated as

$$VA_{Lr} = I_{t,rms}^2 Z_o = \left(\frac{\pi}{2\sqrt{2}}\right)^2 \frac{I_g^2}{\left[\sin\left(\frac{\varphi_{AB}}{2}\right)\right]^2} Z_o. \quad \text{(B.11)}$$

Using the expression of V_{out} from (17), (B.11) can be written as

$$VA_{Lr} = \frac{8n^2}{\pi^2 Z_o} R_{load} \frac{V_{out}^2}{R_{load}} = \frac{R_e}{Z_o} P_{out} = Q P_{out}. \quad \text{(B.12)}$$

VA of L_g is evaluated as

$$VA_{Lg} = I_{R,rms}^2 Z_o = \left(\frac{\pi}{2\sqrt{2}n} I_{load}\right)^2 Z_o = \frac{\pi^2}{8n^2}\left(\frac{V_{out}}{R_{load}}\right)^2 Z_o$$
$$= \frac{Z_o}{\frac{8n^2}{\pi^2} R_{load}} \left(\frac{V_{out}^2}{R_{load}}\right) = \frac{1}{\frac{R_e}{Z_o}} P_{out} = \frac{P_{out}}{Q}. \quad \text{(B.13)}$$

The quality factors presented in (45) are derived here from their basic definition [36]. The quality factor of the load side resonant inductor L_g is derived as

$$Q_L = 2\pi \frac{E_{Lg\_pk} f_o}{P_{out}} \quad \text{(B.14)}$$

where E_{Lg_pk} is the peak energy stored in L_g and is given as

$$E_{Lg\_pk} = \frac{1}{2} L_g (\sqrt{2} I_{R,rms})^2 = L_g I_{R,rms}^2 \quad \text{(B.15)}$$

and from the equivalent circuit of Fig. 5(a), P_{out} can be given as

$$P_{out} = I_{R,rms}^2 R_e. \quad \text{(B.16)}$$

Substituting (B.15) and (B.16) into (B.14) and using definition of ω_o, Z_o and Q from (7), Q_L can be expressed as

$$Q_L = 2\pi f_o \frac{L_g}{R_e} = \frac{Z_o}{R_e} = \frac{1}{Q}. \quad \text{(B.17)}$$

Similarly, the quality factor of the source side resonant inductor L_r can be derived as

$$Q_s = 2\pi \frac{E_{Lr\_pk} f_o}{P_{out}} \quad \text{(B.18)}$$

where E_{Lr_pk} is the peak energy stored in L_r and is given as

$$E_{Lr\_pk} = \frac{1}{2} L_r (\sqrt{2} I_{t,rms})^2 = L_r I_{t,rms}^2. \quad \text{(B.19)}$$

Using the relationship between i_t and i_R from (B.4) and using (B.19) and (7), (B.18) can be further expressed as

$$Q_S = 2\pi f_o \frac{L_r}{R_e}\left(\frac{R_e}{Z_o}\right)^2 = \frac{R_e}{Z_o} = Q. \quad \text{(B.20)}$$

It can be observed from (B.17) and (B.20) that Q_S and Q_L are inverse of each other which means if source side inductor current is more sinusoidal (less in harmonic content), the load side inductor current will be more non-sinusoidal (more harmonic content). This can be observed from the results shown in Fig. 11(a), where at light load, the waveform of i_t is more sinusoidal than waveform of i_R (transformer reflected i_D) when $Q_S = 10$ and $Q_L = 0.1$.

C. Tolerance Analysis

The variation of output voltage due to tolerances in tank component values are shown in Fig. 21 using the analytical expression of V_{out} from (12) and Z_{in} from (13). In Fig. 21, the analytical percentage variation in V_{out} is plotted in solid

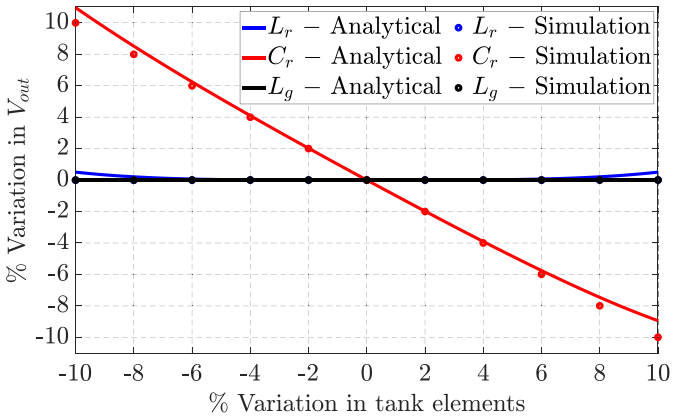

Fig. 21. Percentage variation in dc output voltage (V_{out}) for variation in tank elements. Blue: for variation in L_r, red: for variation in C_r, black: for variation in L_g. Solid lines are for analytical and dots are for simulation results.

lines for variation in L_r (blue), C_r (red) and L_g (black), with one of them varied at a time, keeping the remaining two fixed at their nominal value(s). The tolerance results obtained from MATLAB-PLECS simulation is also shown in the same plot, using dots of corresponding color. It can be seen from this plot in Fig. 21 that there is a little variation in output voltage for variation in tank inductors. However, variation in resonant capacitor has a dominant effect on variation in V_{out}. The results plotted in Fig. 21 are for the lowest load of $P_{out} = 50$ W, where the value of Q is maximum and has highest influence on V_{out} due to component tolerance. With use of a class I ceramic capacitor (C0G, NP0), which is stable over temperature and voltage bias, the capacitance tolerance is within $\pm 5\%$ which translates to variation in V_{out} within $\pm 6\%$, from the result plotted in Fig. 21. This can be taken care of by margin in modulation angle of φ_{AB}, (120° to 180°). Further, since the tolerance is prominent at light loads, active shunt current control circuit [37] can also be utilized at the input source with slight drop of light load efficiency.

REFERENCES

[1] R. L. Steigerwald, "A comparison of half-bridge resonant converter topologies," *IEEE Trans. Power Electron.*, vol. 3, no. 2, pp. 174–182, Apr. 1988.

[2] J. Biela, U. Badstubner, and J. W. Kolar. "Design of a 5-kW, 1-U, 10-kW/dm3 resonant DC–DC converter for telecom applications," *IEEE Trans. Power Electron.*, vol.vol. 24, no.no. 7, pp. 1701–1710, Jul. 2009.

[3] H. Krishnaswami and N. Mohan, "Three-port series-resonant DC–DC converter to interface renewable energy sources with bidirectional load and energy storage ports," *IEEE Trans. Power Electron.*, vol. 24, no. 10, pp. 2289–2297, Oct. 2009.

[4] H. Wang, T. Saha, and R. Zane, "Design considerations for series resonant converters with constant current input," in *Proc. IEEE Energy Convers. Congr. Expo. (ECCE)*, 2016, pp. 1–8.

[5] H. Wang, T. Saha, and R. Zane, "Analysis and design of a series resonant converter with constant current input and regulated output current," in *Proc. IEEE Appl. Power Electron. Conf. Expo. (APEC)*, 2017, pp. 1741–1747.

[6] H. Wang, T. Saha, B. Riar and R. Zane, "Design considerations for current-regulated series-resonant converters with a constant input current," *IEEE Trans. Power Electron.*, vol. 34, no. 1, pp. 141–150, Jan. 2019.

[7] T. Saha, H. Wang, B. Riar, and R. Zane, "Analysis and design of a parallel resonant converter for constant current input to constant voltage output DC-DC converter over wide load range," *2018 Int. Power Electron. Conf.*, 2018, pp. 4074–4079.

[8] T. Saha, A. C. Bagchi, H. Wang, and R. Zane, "Analysis and design of wide range output voltage regulated power supply for underwater constant input current DC distribution system," in *Proc. IEEE 19th Workshop Control Model. for Power Electron. (COMPEL)*, 2018, pp. 1–7.

[9] N. Hasan, H. Wang, T. Saha, and Z. Pantic, "A novel position sensorless power transfer control of lumped coil-based in-motion wireless power transfer systems," in *Proc. IEEE Energy Convers. Congr. Expo. (ECCE)*, Montreal, QC, USA, 2015, pp. 586–593.

[10] S. Yoshida *et al.*, "Underwater wireless power transfer for non-fixed unmanned underwater vehicle in the ocean," in *Proc. IEEE/OES Auton. Underwater Vehicles (AUV)*, Tokyo Japan, 2016, pp. 177–180.

[11] A. C. Bagchi, T. Saha, A. Kamineni, and R. Zane, "Analysis and design of a wireless charger for underwater vehicles fed from a constant current distribution cable," in *Proc. IEEE 19th Workshop Control Model. for Power Electron. (COMPEL)*, 2018, pp. 1–8 .

[12] K. Guo, J. Zhou, H. Sun, and P. Yao, "Design considerations for a position-adaptive contactless underwater power deliver system," *2019 22nd Int. Conf. Elect. Machines Syst. (ICEMS)*, Harbin, China, 2019, pp. 1–6.

[13] M. Borage, S. Tiwari, and S. Kotaiah, "Analysis and design of an LCL-T resonant converter as a constant-current power supply," *IEEE Trans. Ind. Electron.*, vol. 52, no. 6, pp. 1547–1554, Dec. 2005.

[14] M. Borage, S. Tiwari, and S. Kotaiah, "Constant-current, constant-voltage half-bridge resonant power supply for capacitor charging," in *IEE Proc. - Electric Power Appl.*, vol. 153, no. 3, pp. 343–347, May 2006.

[15] M. Borage, S. Tiwari, and S. Kotaiah, "LCL-T resonant converter with clamp diodes: A novel constant-current power supply with inherent constant-voltage limit," *IEEE Trans. Ind. Electron.*, vol. 54, no. 2, pp. 741–746, Apr. 2007.

[16] M. Borage, K. V. Nagesh, M. S. Bhatia, and S. Tiwari, "Design of LCL-T resonant converter including the effect of transformer winding capacitance," *IEEE Trans. Ind. Electron.*, vol. 56, no. 5, pp. 1420–1427, May 2009.

[17] M. B. Borage, K. V. Nagesh, M. S. Bhatia, and S. Tiwari, "Characteristics and design of an asymmetrical duty-cycle-controlled LCL-T resonant converter," *IEEE Trans. Power Electron.*, vol. 24, no. 10, pp. 2268–2275, Oct. 2009.

[18] M. Borage, K. V. Nagesh, M. S. Bhatia, and S. Tiwari, "Resonant immittance converter topologies," *IEEE Trans. Ind. Electron.*, vol. 58, no. 3, pp. 971–978, Mar. 2011.

[19] T. Liang, W. Li, C.-E. Fang, and M. Wang, "Capacitor charging power supply based on LCL-T resonant converter with clamp diodes," in *Proc. 2015 IEEE Region 10 Conf.*, 2015, pp. 1–5.

[20] Q. He, Q. Luo, C. Cao, P. Sun, L. Zhou, and Y. Wei, "A modular multi-channel constant-current LED driver with high frequency AC square voltage bus," in *Proc. IEEE Energy Convers. Congr. Expo. (ECCE)*, Portland, OR, USA, 2018, pp. 4712–4716.

[21] M. Khatua *et al.*, "High-Performance megahertz-frequency resonant DC–DC converter for automotive LED driver applications," *IEEE Trans. Power Electron.*, vol. 35, no. 10, pp. 10396–10412, Oct. 2020.

[22] M. Khatua *et al.*, "High-Performance megahertz-frequency resonant DC-DC converter for automotive LED driver applications," in *Proc. IEEE Energy Convers. Congr. Expo. (ECCE)*, Portland, OR, USA, 2018, pp. 2186–2192.

[23] F. Qu, Z. Wang, H. Song, Y. Chen, and L. Yang, "A study on a cabled seafloor observatory," *IEEE Intell. Syst.*, vol. 30, no. 1, pp. 66–69, Jan./Feb. 2015.

[24] K. Asakawa, J. Kojima, J. Muramatsu, and T. Takada, "Novel current to current converter for mesh-like scientific underwater cable network-concept and preliminary test result," in *Proc. Oceans*, San Diego, CA, USA, 2003, vol. 4, pp. 1868–1873.

[25] A. Mohammadpour, L. Parsa, M. H. Todorovic, R. Lai, R. Datta, and L. Garces, "Series-input parallel-output modular-phase DC–DC converter with soft-switching and high-frequency isolation," *IEEE Trans. Power Electron.*, vol. 31, no. 1, pp. 111–119, Jan. 2016.

[26] K. Modepalli, A. Mohammadpour, T. Li, and L. Parsa, "Three-Phase current-fed isolated DC–DC converter with zero-current switching," *IEEE Trans. Industry Appl.*, vol. 53, no. 1, pp. 242–250, Jan./Feb. 2017.

[27] Z. Zhang, X. Zhou, X. Wang, and T. Wu, "Design, analysis, and modeling of an isolated constant-current to constant-voltage converter in cabled underwater information networks," *Electronics*, vol. 8, pp. 961, 2019.

[28] J. Zeng, J. Liu, J. Yang, and F. Luo, "A voltage-feed high-frequency resonant inverter with controlled current output as a high-frequency AC power source," *IEEE Trans. Power Electron.*, vol. 30, no. 9, pp. 4854–4863, Sep. 2015.

[29] H. Pollock, "Simple constant frequency constant current load-resonant power supply under variable load conditions," *Electron. Lett.*, vol. 33, no. 18, pp. 1505–1506, Aug. 1997.
[30] H. Seidel, "A high power factor tuned class d converter," in *Proc. 19th Annu. IEEE Power Electron. Specialists Conf.*, Kyoto, Japan, 1988, vol. 2, pp. 1038–1042.
[31] R. P. Twiname, D. J. Thrimawithana, U. K. Madawala, and C. A. Baguley, "A new resonant bidirectional DC–DC converter topology," *IEEE Trans. Power Electron.*, vol. 29, no. 9, pp. 4733–4740, Sep. 2014.
[32] S. A. Zapolskiy, A. V. Osipov, I. M. Zhuravlev, and M. E. Khlystunov, "Single-cycle LCL-T resonant converter for solar battery,"*XIV Int. Sci.-Tech. Conf. Actual Problems Electron. Instrum. Eng. (APEIE)*, 2018, pp. 90–93.
[33] T. Saha, H. Wang, and R. Zane, "Zero voltage switching assistance design for DC-DC series resonant converter with constant input current for wide load range," in *Proc. IEEE 18th Workshop Control Model. for Power Electron. (COMPEL)*, Stanford, CA, USA, 2017, pp. 1–5.
[34] T. Saha, H. Wang, B. Riar, and R. Zane, "Analysis of zero voltage switching requirements and passive auxiliary circuit design for DC-DC series resonant converters with constant input current," in *Proc. IEEE 2nd Annu. Southern Power Electron. Conf. (SPEC)*, Auckland, New Zealand, 2016, pp. 1–6.
[35] T. Saha, A. C. Bagchi, and R. Zane, "Time-domain analysis and ZVS assistance design for a DAB LCL-T resonant converter in underwater DC current distribution network," in *Proc. IEEE 21st Workshop Control Model. for Power Electron. (COMPEL)*, Aalborg, Denmark, 2020, accepted for publication.
[36] M. K. Kazimierczuk and D. Czarkowski, in *Resonant Power Converters*. NY, NY, USA: John Wiley & Sons, 2012.
[37] H. Wang, T. Saha, B. Riar, and R. Zane, "Operational study and protection of a series resonant converter with DC current input applied in DC current distribution systems," in *Proc. Int. Power Electron. Conf. (IPEC-Niigata 2018 -ECCE Asia)*, 2018, pp. 4145–4150.

Tarak Saha (Member, IEEE) received the bachelor's degree from Jadavpur University, Kolkata, India in 2008, the master's degree from the Indian Institute of Science, Bangalore, India, in 2010, and the Ph.D. degree from the Utah State University, Logan, UT, USA, in 2020, all in electrical engineering.

At present, he is a Postdoctoral Research Fellow at NSF Engineering Research Center for Advancing Sustainability through Powered Infrastructure for Roadway Electrification (ASPIRE) at Utah State University. Prior to this, he has worked as a power electronics engineer Honeywell in India, Kilby Labs at Texas Instruments Inc., in CA, USA, and National Transportation Research Center (NTRC) at Oak Ridge National Laboratory, TN, USA. His current research interests include resonant power converters and soft switching techniques.

Anindya Chitta Bagchi (Member, IEEE) received the bachelor's degree from Jadavpur University, Kolkata, India, in 2010, the M.Tech degree from the Indian Institute of Technology, Kanpur, India, in 2012, and and the Ph.D. degree from the Utah State University, Logan, UT, USA, in 2020, all in electrical engineering.

He also worked in Bit Mapper in Pune, India for 2.5 years working with electronic systems design. His main research interests include resonant power converters and wireless power transfer systems, for underwater systems and electric vehicle applications.

Regan Andrew Zane (Senior Member, IEEE) received the Ph.D. degree in electrical engineering from the University of Colorado Boulder, Boulder, CO, USA, in 1999.

He is the David G. and Diann L. Sant Endowed Professor with the Department of Electrical and Computer Engineering at Utah State University and the Director of the NSF Engineering Research Center for Advancing Sustainability through Powered Infrastructure for Roadway Electrification (ASPIRE). Prior to joining USU, he was Assistant and Associate Professor with the University of Colorado-Boulder, Colorado Power Electronics Center, and a Research Engineer with GE Global Research Center, Niskayuna, NY, USA. He has coauthored more than 190 peer-reviewed publications and the textbook Digital Control of High-Frequency Switched-Mode Power Converters (New York, NY, USA: Wiley, 2015), and has 24 issued patents. He has recent and ongoing research programs in power electronics for electric vehicle charging infrastructure, including extreme fast charging and static and dynamic wireless charging, battery management systems, dc microgrids, grid-tied and grid-interactive converters, and grid integration of energy storage and renewable energy.

Dr. Zane was recipient of the National Science Foundation Career Award in 2004, the 2005 IEEE Microwave Best Paper Prize, the 2007 and 2009 IEEE Power Electronics Society Transactions Prize Letter Awards, and the 2008 IEEE Power Electronics Society Richard M. Bass Outstanding Young Power Electronics Engineer Award. He was also recipient of the 2006 Inventor of the Year, 2006 Provost Faculty Achievement, 2008 John and Mercedes Peebles Innovation in Teaching, and the 2011 Holland Teaching Awards from the University of Colorado.